RESEARCH ARTICLE

FDTD Analysis of Relativistic Bistatic Polarized Scattering From a High-Speed Moving Dielectric Coated Target

PENGCHENG REN[1,2,3], **LEI KUANG**[1,2,4], **(Member, IEEE),**
JIANJUN GAO[4], **(Senior Member, IEEE), AND QING HUO LIU**[5], **(Fellow, IEEE)**
[1]Shanghai Key Laboratory of Multidimensional Information Processing, East China Normal University, Shanghai 200241, China
[2]Engineering Center of SHMEC for Space Information and GNSS, East China Normal University, Shanghai 200241, China
[3]School of Physics and Electronic Science, East China Normal University, Shanghai 200241, China
[4]School of Communication and Electronic Engineering, East China Normal University, Shanghai 200241, China
[5]Department of Electrical and Computer Engineering, Duke University, Durham, NC 27708, USA

Corresponding author: Lei Kuang (lkuang@ee.ecnu.edu.cn)

ABSTRACT Development of hypersonic aircraft demands relativistic electromagnetic scattering modeling of a high-speed moving dielectric coated object, which is applied to the recognition and tracking of moving stealth object. However, far-zone polarized scatterings from a moving 3D dielectric coated object have not been investigated so far. This paper addresses this problem by combining the finite-difference time-domain method with Lorentz transformation (Lorentz-FDTD). Through Lorentz transformation and the principle of phase invariance, the frequency, propagation direction, magnitude of the incident plane wave and the size of the moving object in the laboratory frame, which is stationary with respect to the free space, are transformed to those in the rest frame that moves with the moving object. The scattered field near the object is solved by the FDTD method with full permittivity and conductivity tensors in the rest frame, then far-zone polarized scattered field is obtained by the implementation of near-to-far field transformation. Through Lorentz transformation for coordinates, the polarized Radar Cross Sections (RCSs) of moving plasma coated objects are solved. Especially, the scattering characteristics of radial radar cross sections of moving objects are discussed. Several numerical experiments are carried out, the efficiency and the accuracy of the proposed method are validated.

INDEX TERMS Finite-difference time domain (FDTD), Lorentz-transformation, high-speed, anisotropic media.

I. INTRODUCTION

With the rapid development of hypersonic aircraft, analysis of electromagnetic scattering of high-speed moving objects has gained great popularity in recent years. The investigation of electromagnetic scattering characteristic of moving conducting targets coated with dielectric that have advantages of good stealth performance, can be applied in detection and feature extraction of high-speed stealth targets. The

The associate editor coordinating the review of this manuscript and approving it for publication was Yi Ren.

finite-difference time-domain (FDTD) algorithm [1], [2] is a leading numerical method for modeling electromagnetic propagation in three-dimensional dielectric object because of its simplicity compared to the analytical method and other numerical algorithms. For the isotropic media, the formula of the FDTD method remain the same as the conventional updated equation. Anisotropic media represent a typical class category of complex materials that have been successfully treated by several extensions of FDTD method. The conventional FDTD method was extended by the implementation of the diagonal anisotropic-medium tensor in [3] for treating

P. Ren et al.: FDTD Analysis of Relativistic Bistatic Polarized Scattering From a High-Speed Moving Dielectric Coated Target

IEEE *Access*

diagonal anisotropic media. In [4], the extension of the FDTD method to nondiagonal anisotropic tensors for both the permittivity and the conductivity was proposed to handle anisotropic media. Several developments of this method were described in [5] by considering the implementation of either second-order or fourth-order approximations for the derivatives to treat lossless anisotropic material. An extension of the FDTD method is considered in [6] by applying electric and magnetic fields as well as electric flux for the treatment of anisotropic dielectric media. In [7] and [8], the extensions of the FDTD method for treating anisotropic dielectrics in both permittivity and permeability were presented. Furthermore, an extension of FDTD method in 3-D cylindrical grids to model fully anisotropic conductive earth media was proposed in [9]. Several efforts have also been made to treat dielectric that are regarded as both anisotropic and frequency dispersive with the FDTD method [8], [10], [11], [12], [13], [14]. However, the above-mentioned algorithms only focus on the electromagnetic analysis of stationary dielectric object.

As the object moves with a high speed, frequency and the amplitude modulation of the scattered wave cannot be neglected. An accurate solution of scattering property of a moving object should be based on Einstein's special relativity theory. Thus, there is a rapidly emerging interest to develop efficient models to simulate moving objects. Over the past several years, the FDTD algorithm have been widely used to analyze scattering properties of moving objects. There are generally two types of methods to solve relativistic scattering from moving objects. One direct solution is to apply the relativistic boundary condition (RBC) [15], [16], [17] at a moving interface between two mediums in the FDTD modeling, namely the RBC-FDTD method. However, it suffers from the numerical instability issue due to electric/magnetic field interpolation on the moving interface at every time step. The other is the Lorentz-FDTD method, transforming incident field to the rest frame of the moving object by a Lorentz transformation, solving scattered fields of the motionless object by the FDTD algorithm in the rest frame, and then transforming scattered fields back to the original laboratory frame. In recent years, the Lorentz-FDTD method, avoiding the field interpolation on the moving interface, has been dominant in solving relativistic scattering problems, due to its numerical stability compared to the RBC-FDTD method. An incident plane wave was introduced into the moving coordinate system, then the double Doppler effects for scattered fields of a moving conducting surface [18] and moving dielectric slabs [19] at different speeds were analyzed by the Lorentz-FDTD method. Reflected and transmitted fields from the moving multilayered dielectric slab illuminated by an impulse source were also discussed by the Lorentz-FDTD method [20]. By applying the Lorentz-FDTD method, bistatic radar cross sections of uniformly moving conducting and dielectric 2-D objects were analyzed and the Doppler effect, that is the function of the incident angle, the velocity vector of the object and the scattering angle, was also given in [21].

The Lorentz-FDTD method was implemented to calculate the scattered fields of a three-dimensional (3-D) complex-shaped object moving at high speed [22]. The scattering fields of a moving conical-shaped object with a vibrational motion were further analyzed by using the Lorentz-FDTD method [23]. By combining the Lorentz transformation with an auxiliary differential equation (ADE) dispersive FDTD method, the reflected and transmitted waves by a moving 2-D LHM slab were investigated [24]. Since the research object is a moving 2-D LHM slab, the cross-polarized RCS cannot be obtained. Combing the boundary perturbation technique with Lorentz transformation, bistatic scattering coefficients of moving slightly rough surfaces have been studied in [25]. The radial scattering cross sections which owe their existence solely to the scatter's motion are also presented. However, it is difficult to obtain exact scattering solutions for general moving objects with arbitrary shapes and compositions by the aforementioned asymptotic method in [25]. So far, the polarized scatterings of moving 3-D dielectric coated targets have not been addressed.

In this paper, we combine the FDTD method with Lorentz transformation to calculate relativistic polarized scatterings from a moving 3D dielectric object, especially the moving 3D anisotropic media coated target. In section II, the transformation of spatial size and incident plane wave between the rest frame and the laboratory frame is introduced. And we briefly summarize the FDTD method which is extended to handle the anisotropic material with full permittivity and conductivity tensor and describe the implementation of the extended FDTD method to calculate the near field of the moving 3D dielectric target in the rest frame. Meanwhile, the far-zone scattered field of a moving target and RCS of a moving target are presented, respectively. In section III, the reflection coefficients of a moving slab are proposed to verify the efficiency and accuracy of the proposed method. And polarized RCSs of moving 3D dielectric coated objects are presented by the implementation of the proposed method. Eventually, the scattering characteristics of radial radar cross sections are discussed. Finally, conclusions are presented in section IV.

II. THEORY AND FORMULATION

We combine the Lorentz transformation with the FDTD method to analyze far-zone relativistic scattering of a three-dimensional high-speed dielectric coated object in this paper. Consider that the laboratory frame Ω is stationary with respect to the free space, and the rest frame Ω' moves uniformly along $+x$ axis with velocity v relative to the laboratory frame Ω. Thus, the moving target seems to be stationary in the frame Ω'. As shown in Fig. 1, the coordinate axes of the laboratory frame Ω and the rest frame Ω' are parallel, with their origins coinciding at time $t = 0$.

A. TRANSFORMATION OF INCIDENT PLANE WAVE
In the FDTD method, the spatial increments of Δx, Δy, and Δz are used in the laboratory frame Ω. The spatial increments

IEEE *Access*

P. Ren et al.: FDTD Analysis of Relativistic Bistatic Polarized Scattering From a High-Speed Moving Dielectric Coated Target
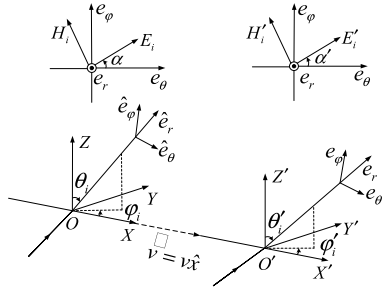
FIGURE 1. Sketch graph of the laboratory frame and the rest frame.

in the rest frame Ω' are represented by corresponding primed quantities $\Delta x'$, $\Delta y'$, and $\Delta z'$.

Consider the object moves along the x axis with the velocity of v. Applying the Lorentz transformation, the transformation relations between spatial increments in the Ω and Ω' frames can be rewritten as:

$$\Delta x' = \gamma \Delta x \tag{1a}$$

$$\Delta y' = \Delta y \tag{1b}$$

$$\Delta z' = \Delta z \tag{1c}$$

$$\gamma = 1 \Big/ \sqrt{1 - \beta^2} \tag{1d}$$

$$\beta = v/c \tag{1e}$$

where, c is the velocity of the light in vacuum.

As shown in Fig. 1, a plane monochromatic wave incident upon the moving target in the laboratory frame can be given by:

$$\vec{E}_i = \left(E_{ix}\hat{x} + E_{iy}\hat{y} + E_{iz}\hat{z} \right) \exp \left\{ j \left(\vec{k}_i \cdot \vec{r} - \omega_i t \right) \right\} \tag{2a}$$

$$\vec{H}_i = \left(H_{ix}\hat{x} + H_{iy}\hat{y} + H_{iz}\hat{z} \right) \exp \left\{ j \left(\vec{k}_i \cdot \vec{r} - \omega_i t \right) \right\} \tag{2b}$$

where

$$E_{ix} = E_0 \left(-\sin\varphi_i \sin\alpha + \cos\theta_i \cos\varphi_i \cos\alpha \right) \tag{2c}$$

$$E_{iy} = E_0 \left(\cos\varphi_i \sin\alpha + \cos\theta_i \sin\varphi_i \cos\alpha \right) \tag{2d}$$

$$E_{iz} = -E_0 \sin\theta_i \cos\alpha \tag{2e}$$

$$H_{ix} = E_0 \big/ Z_0 \left(-\sin\varphi_i \cos\alpha - \cos\theta_i \cos\varphi_i \sin\alpha \right) \tag{2f}$$

$$H_{iy} = E_0 \big/ Z_0 \left(\cos\varphi_i \cos\alpha - \cos\theta_i \sin\varphi_i \sin\alpha \right) \tag{2g}$$

$$H_{iz} = E_0 \big/ Z_0 \sin\theta_i \sin\alpha \tag{2h}$$

$$\vec{k}_i = k_i\hat{x} \sin\theta_i \cos\varphi_i + k_i\hat{y} \sin\theta_i \sin\varphi_i + k_s\hat{z} \cos\theta_i \tag{2i}$$

As shown in Fig. 1, α denotes the polarization angle of the incident field; θ_i and φ_i are the propagation angles; $\vec{r} = x\hat{x} + y\hat{y} + z\hat{z}$ is the position vector; k_i is the incident-wave wavenumber; ω_i denotes the incident-wave angular frequency; Z_0 represents the intrinsic impendence in free space; E_0 denotes the amplitude of an incident electric field and $j = \sqrt{-1}$.

By applying Lorentz transformation and the principle of phase invariance, the frequency, propagation direction and magnitude of the incident wave in Ω' are deduced. Replacing

each quantity of (2a) - (2b) with the corresponding primed one, the incident wave in Ω' are expressed as:

$$\vec{E}'_i = \left(E'_{ix}\hat{x} + E'_{iy}\hat{y} + E'_{iz}\hat{z} \right) \exp \left\{ j \left(\vec{k}'_i \cdot \vec{r}' - \omega'_i t' \right) \right\} \tag{3a}$$

$$\vec{H}'_i = \left(H'_{ix}\hat{x} + H'_{iy}\hat{y} + H'_{iz}\hat{z} \right) \exp \left\{ j \left(\vec{k}'_i \cdot \vec{r}' - \omega'_i t' \right) \right\} \tag{3b}$$

In the case that the target moves along the $+x$ axis with the velocity v, relations between corresponding unprimed and primed quantities of the incident wave are presented as

$$E'_0 = E_0 \gamma \left(1 - \beta \sin\theta_i \cos\varphi_i \right) \tag{4a}$$

$$k'_i = k_i \gamma \left(1 - \beta \sin\theta_i \cos\varphi_i \right) \tag{4b}$$

$$\omega'_i = \omega_i \gamma \left(1 - \beta \sin\theta_i \cos\varphi_i \right) \tag{4c}$$

$$\sin\theta'_i = \frac{\sqrt{\gamma^2 (\sin\theta_i \cos\varphi_i - \beta)^2 + \sin^2\theta_i \sin^2\varphi_i}}{\gamma (1 - \beta \sin\theta_i \cos\varphi_i)} \tag{4d}$$

$$\cos\theta'_i = \frac{\cos\theta_i}{\gamma (1 - \beta \sin\theta_i \cos\varphi_i)} \tag{4e}$$

$$\sin\varphi'_i = \frac{\sin\theta_i \sin\varphi_i}{\sqrt{\gamma^2 (\sin\theta_i \cos\varphi_i - \beta)^2 + \sin^2\theta_i \sin^2\varphi_i}} \tag{4f}$$

$$\cos\varphi'_i = \frac{\gamma (\sin\theta_i \cos\varphi_i - \beta)}{\sqrt{\gamma^2 (\sin\theta_i \cos\varphi_i - \beta)^2 + \sin^2\theta_i \sin^2\varphi_i}} \tag{4g}$$

$$\sin\alpha' = \frac{\gamma (\sin\theta_i \sin\alpha - \beta \cos\varphi_i \sin\alpha - \beta \sin\varphi_i \cos\theta_i \cos\alpha)}{\sqrt{\gamma^2 (\sin\theta_i \cos\varphi_i - \beta)^2 + \sin^2\theta_i \sin^2\varphi_i}} \tag{4h}$$

$$\cos\alpha' = \frac{\gamma (\sin\theta_i \cos\alpha - \beta \cos\varphi_i \cos\alpha + \beta \sin\varphi_i \cos\theta_i \sin\alpha)}{\sqrt{\gamma^2 (\sin\theta_i \cos\varphi_i - \beta)^2 + \sin^2\theta_i \sin^2\varphi_i}} \tag{4i}$$

After acquiring the transformations between the two frames, the extension of FDTD algorithm for anisotropic media with full permittivity and conductivity tensors can be applied to solve the near-zone scattered fields of a moving dielectric coated object in the rest frame Ω', since it is relatively motionless in Ω'. The FDTD computation domain is divided into Yee grids and truncated by convolutional perfectly matched layer (CPML) for the absorption of the outward-propagating waves. The incident plane wave transformed from the laboratory frame to the rest frame, is introduced to excite the target by the Total-field scattered-field (TF-SF) connecting boundary technology. The computational domain is divided into total-field domain and scattered field domain by the connecting boundary. The total-field domain, including both scattered field of the target and incident field, is enclosed by the connecting boundary. The scattered-field domain is outside the connecting boundary, which only contains of scattered field. By employing the extended FDTD iterative formulas, near-zone scattered field of the target in the rest frame Ω' can be acquired.

P. Ren et al.: FDTD Analysis of Relativistic Bistatic Polarized Scattering From a High-Speed Moving Dielectric Coated Target

IEEE *Access*

B. FDTD METHOD FOR ANISOTROPIC MATERIAL

The material used in this paper can be divided into the isotropic medium and the anisotropic medium, where for the isotropic medium, the updated equation reverts to the conventional FDTD scheme. In this section, we only discuss the FDTD updated equation for anisotropic material in the rest frame Ω'.

In anisotropic material, the constructive relations are written as:

$$\vec{D} = \boldsymbol{\varepsilon} \cdot \vec{E} \tag{5a}$$

$$\vec{J} = \boldsymbol{\sigma} \cdot \vec{E} \tag{5b}$$

in which $\boldsymbol{\varepsilon}$ and $\boldsymbol{\sigma}$ are tensors. In this paper, the nonmagnetic materials are considered. For this case, the Maxwell's curl equations are

$$\nabla \times \vec{E} = -\frac{\partial \vec{B}}{\partial t} - \vec{J}_m = -\mu \frac{\partial \vec{H}}{\partial t} - \sigma_m \vec{H} \tag{6a}$$

$$\nabla \times \vec{H} = \frac{\partial \vec{D}}{\partial t} + \vec{J} = \boldsymbol{\varepsilon} \cdot \frac{\partial \vec{E}}{\partial t} + \boldsymbol{\sigma} \cdot \vec{E} \tag{6b}$$

Consider the central difference for the temporal derivatives and the semi-implicit approximation. Here, we can obtain

$$\nabla \times \vec{H}^{n+1/2} = \boldsymbol{\varepsilon} \cdot \frac{\vec{E}^{n+1} - \vec{E}^n}{\Delta t'} + \boldsymbol{\sigma} \cdot \frac{\vec{E}^{n+1} + \vec{E}^n}{2}$$
$$= \left(\frac{\boldsymbol{\varepsilon}}{\Delta t'} + \frac{\boldsymbol{\sigma}}{2}\right) \cdot \vec{E}^{n+1} - \left(\frac{\boldsymbol{\varepsilon}}{\Delta t'} - \frac{\boldsymbol{\sigma}}{2}\right) \cdot \vec{E}^n \tag{7}$$

where $\Delta t'$ used in the above equation denotes the time step in the rest frame, which can be expressed as

$$\Delta t' = 1 \bigg/ \left(c\sqrt{1 \big/ (\Delta x')^2 + 1 \big/ (\Delta y')^2 + 1 \big/ (\Delta z')^2} \right) \tag{8}$$

Then, the update equation of the electric field can be written as

$$\vec{E}^{n+1} = \mathbf{P} \cdot \vec{E}^n + \mathbf{Q} \cdot \nabla \times \vec{H}^{n+1/2} \tag{9}$$

where

$$\mathbf{P} = \left(\frac{\boldsymbol{\varepsilon}}{\Delta t'} + \frac{\boldsymbol{\sigma}}{2}\right)^{-1} \cdot \left(\frac{\boldsymbol{\varepsilon}}{\Delta t'} - \frac{\boldsymbol{\sigma}}{2}\right) \tag{10a}$$

$$\mathbf{Q} = \left(\frac{\boldsymbol{\varepsilon}}{\Delta t'} + \frac{\boldsymbol{\sigma}}{2}\right)^{-1} \tag{10b}$$

Modify the above equation (9) into the component form, which can be presented as

$$\begin{pmatrix} E_x^{n+1} \\ E_y^{n+1} \\ E_z^{n+1} \end{pmatrix} = \mathbf{P} \begin{pmatrix} E_x^n \\ E_y^n \\ E_z^n \end{pmatrix} + \mathbf{Q} \begin{pmatrix} \dfrac{\partial H_z^{n+1/2}}{\partial y} - \dfrac{\partial H_y^{n+1/2}}{\partial z} \\[2mm] \dfrac{\partial H_x^{n+1/2}}{\partial z} - \dfrac{\partial H_z^{n+1/2}}{\partial x} \\[2mm] \dfrac{\partial H_y^{n+1/2}}{\partial x} - \dfrac{\partial H_x^{n+1/2}}{\partial y} \end{pmatrix} \tag{11}$$

Due to the similar form of the E_y and E_z components, only the E_x component is considered in this paper, which can be written as

$$E_x^{n+1}\left(i + \frac{1}{2}, j, k\right)$$
$$= P_{xx} E_x^n\left(i + \frac{1}{2}, j, k\right) + P_{xy} E_y^n\left(i + \frac{1}{2}, j, k\right)$$
$$+ P_{xz} E_z^n\left(i + \frac{1}{2}, j, k\right) + Q_{xx}\left(\frac{\partial H_z}{\partial y} - \frac{\partial H_y}{\partial z}\right)_{i+1/2,j,k}^{n+1/2}$$
$$+ Q_{xy}\left(\frac{\partial H_x}{\partial z} - \frac{\partial H_z}{\partial x}\right)_{i+1/2,j,k}^{n+1/2}$$
$$+ Q_{xz}\left(\frac{\partial H_y}{\partial x} - \frac{\partial H_x}{\partial y}\right)_{i+1/2,j,k}^{n+1/2} \tag{12}$$

Considering the inconsistency between the discrete point positions of the E and H in the above equation and the corresponding component node position in the Yee grid, the electric field quantities are interpolated from neighboring quantities as follows:

$$E_y^n\left(i + \frac{1}{2}, j, k\right)$$
$$= \frac{1}{4}\left(E_y^n\left(i+1, j+\frac{1}{2}, k\right) + E_y^n\left(i, j+\frac{1}{2}, k\right)\right.$$
$$\left. + E_y^n\left(i+1, j-\frac{1}{2}, k\right) + E_y^n\left(i, j-\frac{1}{2}, k\right)\right) \tag{13a}$$

$$E_z^n\left(i + \frac{1}{2}, j, k\right)$$
$$= \frac{1}{4}\left(E_z^n\left(i+1, j, k+\frac{1}{2}\right) + E_z^n\left(i, j, k+\frac{1}{2}\right)\right.$$
$$\left. + E_z^n\left(i+1, j, k-\frac{1}{2}\right) + E_z^n\left(i, j, k-\frac{1}{2}\right)\right) \tag{13b}$$

The spatial derivatives of the magnetic field can be presented as:

$$\frac{\partial H_y^{n+1/2}\left(i + \frac{1}{2}, j, k\right)}{\partial x}$$
$$= \frac{1}{4\Delta x'}\left(H_y^{n+1/2}\left(i+\frac{3}{2}, j, k+\frac{1}{2}\right) + H_y^{n+1/2}\left(i+\frac{3}{2}, j, k-\frac{1}{2}\right)\right.$$
$$\left. - H_y^{n+1/2}\left(i-\frac{1}{2}, j, k+\frac{1}{2}\right) - H_y^{n+1/2}\left(i-\frac{1}{2}, j, k-\frac{1}{2}\right)\right) \tag{14a}$$

$$\frac{\partial H_z^{n+1/2}\left(i + \frac{1}{2}, j, k\right)}{\partial x}$$
$$= \frac{1}{4\Delta x'}\left(H_z^{n+1/2}\left(i+\frac{3}{2}, j+\frac{1}{2}, k\right) + H_z^{n+1/2}\left(i+\frac{3}{2}, j-\frac{1}{2}, k\right)\right.$$
$$\left. - H_z^{n+1/2}\left(i-\frac{1}{2}, j+\frac{1}{2}, k\right) - H_z^{n+1/2}\left(i-\frac{1}{2}, j-\frac{1}{2}, k\right)\right) \tag{14b}$$

IEEE Access

P. Ren et al.: FDTD Analysis of Relativistic Bistatic Polarized Scattering From a High-Speed Moving Dielectric Coated Target

$$\frac{\partial H_x^{n+1/2}\left(i+\frac{1}{2},j,k\right)}{\partial y}$$

$$= \frac{1}{4\Delta y'}\left(H_x^{n+1/2}\left(i+1,j+\frac{1}{2},k+\frac{1}{2}\right)\right.$$

$$+ H_x^{n+1/2}\left(i,j+\frac{1}{2},k+\frac{1}{2}\right)$$

$$+ H_x^{n+1/2}\left(i+1,j+\frac{1}{2},k-\frac{1}{2}\right)+H_x^{n+1/2}\left(i,j+\frac{1}{2},k-\frac{1}{2}\right)$$

$$- H_x^{n+1/2}\left(i+1,j-\frac{1}{2},k+\frac{1}{2}\right)-H_x^{n+1/2}\left(i,j-\frac{1}{2},k+\frac{1}{2}\right)$$

$$\left.- H_x^{n+1/2}\left(i+1,j-\frac{1}{2},k-\frac{1}{2}\right)-H_x^{n+1/2}\left(i,j-\frac{1}{2},k-\frac{1}{2}\right)\right)$$

(14c)

$$\frac{\partial H_x^{n+1/2}\left(i+\frac{1}{2},j,k\right)}{\partial z}$$

$$= \frac{1}{4\Delta z'}\left(H_x^{n+1/2}\left(i+1,j+\frac{1}{2},k+\frac{1}{2}\right)\right.$$

$$+ H_x^{n+1/2}\left(i,j+\frac{1}{2},k+\frac{1}{2}\right)$$

$$+ H_x^{n+1/2}\left(i+1,j-\frac{1}{2},k+\frac{1}{2}\right)+H_x^{n+1/2}\left(i,j-\frac{1}{2},k+\frac{1}{2}\right)$$

$$- H_x^{n+1/2}\left(i+1,j+\frac{1}{2},k-\frac{1}{2}\right)-H_x^{n+1/2}\left(i,j+\frac{1}{2},k-\frac{1}{2}\right)$$

$$\left.- H_x^{n+1/2}\left(i+1,j-\frac{1}{2},k-\frac{1}{2}\right)-H_x^{n+1/2}\left(i,j-\frac{1}{2},k-\frac{1}{2}\right)\right)$$

(14d)

The formulation of $\partial H_x/\partial y$ and $\partial H_y/\partial x$ remain the same as the conventional FDTD equation. Substituting (13a)-(13b) and (14a)-(14d) into (12), the complete expression of E_x can be obtained. And similar expression of E_y and E_z can easily be yielded by referring to the expression of E_x.

C. TRANSFORMATION OF THE SCATTERED FIELD

After completing the calculation of the electric and magnetic fields near the dielectric target, we apply the near-to-far field transformation technique to acquire far-zone scattered field of the target in the rest frame. As shown in Fig. 2, we set a closed virtual surface S_v surrounding the target in the scattered-field region. According to the equivalence theorem, far-zone scattered field of the target can be yielded in terms of equivalent surface electric current $\vec{J}'^e$ and equivalent surface magnetic current $\vec{J}'^m$.

$$\vec{J}'^e = \hat{n} \times \vec{H}' \tag{15a}$$

$$\vec{J}'^m = -\hat{n} \times \vec{E}' \tag{15b}$$

where $\hat{n}$ is the unit outward normal vector of the S_v in the rest frame Ω'. Once the electric and magnetic fields near the target are calculated by the FDTD method, amplitude and phase data of $\vec{J}'^e$ and $\vec{J}'^m$ can be obtained by (15a) - (15b).
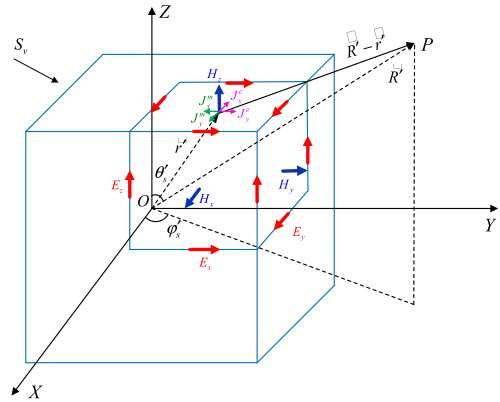
FIGURE 2. Near-to-far field extrapolation.

In the frequency domain, the far-zone scattered electric and magnetic field of the target are obtained from

$$\vec{E}'_s = j\vec{k}'_s \times \vec{F} - j\omega'_s\mu\vec{A} - \frac{\vec{k}'_s}{j\omega'_s\varepsilon}\left(\vec{k}'_s \cdot \vec{A}\right) \tag{16a}$$

$$\vec{H}'_s = -j\vec{k}'_s \times \vec{A} - j\omega'_s\varepsilon\vec{F} - \frac{\vec{k}'_s}{j\omega'_s\mu}\left(\vec{k}'_s \cdot \vec{F}\right) \tag{16b}$$

where, $\vec{k}'_s$ is scattered wave vector; ω'_s denotes the angular frequency of the scattered wave propagating in the rest frame, which is equal to ω'_i. Here, vector potentials $\vec{A}$ and $\vec{F}$ for the three-dimensional case are defined as

$$\vec{A} = \frac{exp\left(-jk'_sR'\right)}{4\pi R'}\int_{S_v}\vec{J}'^e(\vec{r}')exp\left(jk'_s\hat{e}_{R'} \times \vec{r}'\right)ds \tag{17a}$$

$$\vec{F} = \frac{exp\left(-jk'_sR'\right)}{4\pi R'}\int_{S_v}\vec{J}'^m(\vec{r}')exp\left(jk'_s\hat{e}_{R'} \times \vec{r}'\right)ds \tag{17b}$$

where $k'_s = k'_i$ scattered wave wavenumber in the rest frame; R' is the distance from the origin O to the observation point P; $\hat{e}_{R'}$ denotes the unit vector directed to the observation point; the vector $\vec{r}'$ denotes the position of source point on the virtual surface S_v, as shown in Fig. 2.

Since the FDTD calculation is carried out in Cartesian coordinates system, scattered electric/magnetic field components in (16a) - (16b) can be expressed corresponding to Cartesian coordinates system as follows (18a)–(18f), shown at the bottom of the next page, where

$$A_\zeta = \frac{exp\left(-jk'_sR'\right)}{4\pi R'}\int_{S_v}J'^e_\zeta exp\left(jk'_sx'sin\theta'_scos\varphi'_s\right.$$
$$\left.+ jk'_sy'sin\theta'_ssin\varphi'_s + jk'_sz'cos\theta'_s\right)ds \tag{19a}$$

$$F_\zeta = \frac{exp\left(-jk'_sR'\right)}{4\pi R'}\int_{S_v}J'^m_\zeta exp\left(jk'_sx'sin\theta'_scos\varphi'_s\right.$$
$$\left.+ jk'_sy'sin\theta'_ssin\varphi'_s + jk'_sz'cos\theta'_s\right)ds \tag{19b}$$

Here $\zeta = x, y, z$ represents the three components of the Cartesian coordinates, respectively. Substituting (19a) - (19b) into (18a) - (18f), the far-zone scattered electric/magnetic fields in the rest frame can be calculated.

In the case that the object moves along $+x$ axis with the velocity of v, applying Lorentz transformation formulas for

P. Ren et al.: FDTD Analysis of Relativistic Bistatic Polarized Scattering From a High-Speed Moving Dielectric Coated Target

IEEE *Access*

field vectors, far-zone scattered electric fields in the rest frame Ω' can be transformed back to the laboratory frame Ω in the form as follows:

$$E_{sx} = E'_{sx} \tag{20a}$$

$$E_{sy} = \gamma \left(E'_{sy} + v \cdot \mu \cdot H'_{sz} \right) \tag{20b}$$

$$E_{sz} = \gamma \left(E'_{sz} - v \cdot \mu \cdot H'_{sy} \right) \tag{20c}$$

D. POLARIZED RCS OF THE MOVING OBJECT

The polarized scattered field components are usually considered in the electromagnetic scattering problem, which are perpendicular and parallel to the plane of scatter, respectively. However, in doing so, the expressions for the RCS of the moving target cannot be handled. As an alternative way presented in the reference [25], the scattered electric field $\vec{E}_s$ to the observation point P in the Ω is analyzed into the field components E_{sh}, E_{sv}, and E_{sr} corresponding to the spherical coordinates system $(O_G, r(t), \theta_s(t), \varphi_s(t))$, as shown in Fig. 3. The system (O_G, X_G, Y_G, Z_G) moving with the object is the Galilean counterpart of the system (O', X', Y', Z') considered in the Ω'. Note that the motion of the object brings about the new component E_{sr}, although it is zero for a stationary object. Thus, three polarized electric field components transformed from the rectangular coordinates system (O, X, Y, Z) to the sphere coordinates system $(O_G, r(t), \theta_s(t), \varphi_s(t))$ are written as:

$$\begin{pmatrix} E_{sh} \\ E_{sv} \\ E_{sr} \end{pmatrix} = \begin{pmatrix} -\sin\varphi_s(t) & \cos\varphi_s(t) & 0 \\ \cos\theta_s(t)\cos\varphi_s(t) & \cos\theta_s(t)\sin\varphi_s(t) & -\sin\theta_s(t) \\ \sin\theta_s(t)\cos\varphi_s(t) & \sin\theta_s(t)\sin\varphi_s(t) & \cos\theta_s(t) \end{pmatrix}$$
$$\times \begin{pmatrix} E_{sx} \\ E_{sy} \\ E_{sz} \end{pmatrix} \tag{21}$$

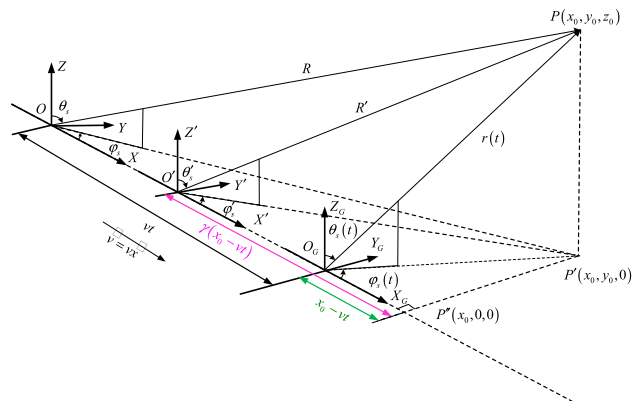where E_{sx}, E_{sy}, and E_{sz} are derived from (20a) - (20c).

FIGURE 3. Scattering geometry.

As shown in Fig. 3, R is the distance from the origin O to the observation point $P(x_0, y_0, z_0)$.

The electromagnetic power scattered to $P(x_0, y_0, z_0)$ is represented by the three-dimensional bistatic RCS of the moving target.

$$\text{RCS} = \lim_{R \to \infty} 10 \lg \left(4\pi R^2 \left| \frac{E_q}{E_p} \right|^2 \right) \text{ (dBsm)} \tag{22}$$

where E_q and E_p stand for the q (v, h, r)-polarized scattered fields and p (v, h)-polarized incident fields, respectively. The subscript v and h represent the vertical polarization and horizontal polarization, respectively. And the subscript r denotes the radial component of the scattering. It can be seen that the expressions of $|E_q|$ include quantities R', θ'_s, and φ'_s considered in the Ω'. The key step in the solution of various polarized RCS of the moving target is to derive the relations between R', θ'_s, and φ'_s in the rest frame and R, θ_s, and φ_s in the

$$E'_{sx} = jk'_s \left\{ \begin{array}{l} F_z \sin\theta'_s \sin\varphi'_s - F_y \cos\theta'_s + Z_0 \left(\sin^2\theta'_s \cos^2\varphi'_s - 1 \right) A_x \\ + Z_0 \sin^2\theta'_s \sin\varphi'_s \cos\varphi'_s A_y + Z_0 \sin\theta'_s \cos\theta'_s \cos\varphi'_s A_z \end{array} \right\} \tag{18a}$$

$$E'_{sy} = jk'_s \left\{ \begin{array}{l} F_x \cos\theta'_s - F_z \sin\theta'_s \cos\varphi'_s + Z_0 \left(\sin^2\theta'_s \sin^2\varphi'_s - 1 \right) A_y \\ + Z_0 \sin^2\theta'_s \sin\varphi'_s \cos\varphi'_s A_x + Z_0 \sin\theta'_s \cos\theta'_s \sin\varphi'_s A_z \end{array} \right\} \tag{18b}$$

$$E'_{sz} = jk'_s \left\{ \begin{array}{l} F_y \sin\theta'_s \cos\varphi'_s - F_x \sin\theta'_s \sin\varphi'_s + Z_0 \left(\cos^2\theta'_s - 1 \right) A_z \\ + Z_0 \sin\theta'_s \cos\theta'_s \cos\varphi'_s A_x + Z_0 \sin\theta'_s \cos\theta'_s \sin\varphi'_s A_y \end{array} \right\} \tag{18c}$$

$$H'_{sx} = jk'_s \left\{ \begin{array}{l} -A_z \sin\theta'_s \sin\varphi'_s + A_y \cos\theta'_s + \dfrac{1}{Z_0} \left(\sin^2\theta'_s \cos^2\varphi'_s - 1 \right) F_x \\ + \dfrac{1}{Z_0} \sin^2\theta'_s \sin\varphi'_s \cos\varphi'_s F_y + \dfrac{1}{Z_0} \sin\theta'_s \cos\theta'_s \cos\varphi'_s F_z \end{array} \right\} \tag{18d}$$

$$H'_{sy} = jk'_s \left\{ \begin{array}{l} -A_x \cos\theta'_s + A_z \sin\theta'_s \cos\varphi'_s + \dfrac{1}{Z_0} \left(\sin^2\theta'_s \sin^2\varphi'_s - 1 \right) F_y \\ + \dfrac{1}{Z_0} \sin^2\theta'_s \sin\varphi'_s \cos\varphi'_s F_x + \dfrac{1}{Z_0} \sin\theta'_s \cos\theta'_s \sin\varphi'_s F_z \end{array} \right\} \tag{18e}$$

$$H'_{sz} = jk'_s \left\{ \begin{array}{l} -A_y \sin\theta'_s \cos\varphi'_s + A_x \sin\theta'_s \sin\varphi'_s + \dfrac{1}{Z_0} \left(\cos^2\theta'_s - 1 \right) F_z \\ + \dfrac{1}{Z_0} \sin\theta'_s \cos\theta'_s \cos\varphi'_s F_x + \dfrac{1}{Z_0} \sin\theta'_s \cos\theta'_s \sin\varphi'_s F_y \end{array} \right\} \tag{18f}$$

IEEE Access

P. Ren et al.: FDTD Analysis of Relativistic Bistatic Polarized Scattering From a High-Speed Moving Dielectric Coated Target

laboratory frame, which can be solved by applying the special homogeneous Lorentz transformation for coordinates.

When the target moves along the $+x$ axis with the velocity of v, as shown in Fig. 3, the distance from O_G to P'' is $\overline{O_G P''} = (x_0 - vt)$, due to the Galilean transformation. According to the Lorentz contraction effect, $\overline{O'P''} = \gamma (x_0 - vt)$. When R approaches to infinity, as shown in Fig. 3, we find that

$$\lim_{R \to \infty} r(t) = R \tag{23a}$$

$$\lim_{R \to \infty} \theta_s(t) = \theta_s \tag{23b}$$

$$\lim_{R \to \infty} \varphi_s(t) = \varphi_s \tag{23c}$$

According to the relation between the triangle $P'OP''$ and the triangle $P'O_GP''$, it can be proven that

$$\lim_{R \to \infty} \sin \varphi_s' = \sin \varphi_s \frac{\sqrt{1 - \beta^2}}{\sqrt{1 - \beta^2 \sin^2 \varphi_s}} \tag{24a}$$

$$\lim_{R \to \infty} \cos \varphi_s' = \cos \varphi_s \frac{1}{\sqrt{1 - \beta^2 \sin^2 \varphi_s}} \tag{24b}$$

According to the relation between the triangle $PO'P'$ and the triangle PO_GP', the transformation relations between θ_s, R, and θ_s', R' are given by

$$\lim_{R \to \infty} \cos \theta_s' = \cos \theta_s \frac{\sqrt{1 - \beta^2}}{\sqrt{1 - \beta^2 \left(\cos^2 \theta_s + \sin^2 \theta_s \sin^2 \varphi_s \right)}} \tag{24c}$$

$$\lim_{R \to \infty} \sin \theta_s' = \sin \theta_s \frac{\sqrt{1 - \beta^2 \sin^2 \varphi_s}}{\sqrt{1 - \beta^2 \left(\cos^2 \theta_s + \sin^2 \theta_s \sin^2 \varphi_s \right)}} \tag{24d}$$

$$\lim_{R \to \infty} \frac{R}{R'} = \frac{\sqrt{1 - \beta^2}}{\sqrt{1 - \beta^2 \left(\cos^2 \theta_s + \sin^2 \theta_s \sin^2 \varphi_s \right)}} \tag{24e}$$

Substituting (24a)-(24e), (18a)-(18e), (19a)-(19b), (20a)-(20c), and (21) into equation (22), the polarized bistatic RCS of the moving object are obtained. It should be noted that new component E_{sr} that results from the motion of the object, while it is zero for the motionless object.

III. NUMERICAL RESULTS
In this section, the performance of the proposed scheme is demonstrated by several numerical cases. The first case focused on the reflection coefficient of a moving dielectric slab to demonstrate the accuracy and validity of the proposed method. The second case focuses on the bistatic RCS (Radar Cross Section) of a moving isotropic material coated targets with perfectly conducting (PEC) backing medium. And the third and fourth cases discuss the far-zone bistatic polarized scatterings from a moving anisotropic material coated cylinder with PEC backing medium and a moving complex cone-shaped target with PEC backing medium, respectively.
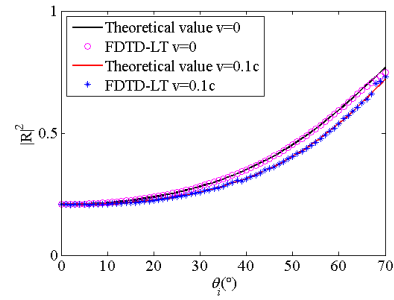

FIGURE 4. Reflection coefficient of the moving slab.

Eventually, numerical results are obtained to discuss the scattering characteristics of the radial radar cross section. Meanwhile, we assume that all targets simulated in this section move uniformly along the $+x$ coordinate axis.

A. REFLECTION OF A MOVING DIELECTRIC SLAB
Reflection coefficients of a moving dielectric slab are calculated by using the proposed method. Suppose the slab with relative permittivity $\varepsilon_r = 2.7$, relative permeability $\mu_r = 1$ and a thickness of $d = 0.005$ m. To validate the proposed method, the theoretical results for the same model are considered.

A plane wave with electric field linearly polarized along the y coordinate axis is incident on the front surface of the slab. We numerically solved reflection coefficients for incidence angles between $0°$ and $70°$. Fig. 4 gives reflection coefficient of the slab moving parallel to the interface along the $+x$ axis with a constant velocity of $v = 0.1c$ m/s, and is compared with the static case. It can be seen that the reflection coefficient decreases due to the high-speed motion of the slab, especially when the incident angle is greater than $30°$. Simultaneously, the theoretical results are solved by using formulas presented in [26]. A perfect agreement is observed between the theoretical and simulated results, proving the validity of the proposed method.

B. RCS OF A MOVING ISOTROPIC MATERIAL COATED CYLINDER
In this case, the bistatic scatterings from an isotropic media coated cylinder is presented. For the isotropic material coated cylinder, the dimensions of the cylinder are $r = 0.1$ m and $h = 0.4$ m. The thickness of the coating material is 0.01 m. The constitutive parameters of the coated material are $\varepsilon_r = (4, -1)$ and $\mu_r = (1, 0)$. We calculate near-zone scattered field near the object by the FDTD method in the rest frame Ω', where the size of the object is changed according to (1a)-(1c). A plane wave of the frequency 3 GHz with unit amplitude is introduced to excite the object at $(\theta_i = 90°, \varphi_i = 90°)$, as shown in Fig. 1, by applying the total-field/scattered-field (TF/SF) boundary conditions. Also, the parameters of the incident wave are transformed in terms of (2c)-(2i) in the rest frame Ω'.

Bistatic RCS versus θ_s for the target with velocities of $v = 0, 0.00001c$ (about Mach 8.82), $0.01c$, and $0.1c$ m/s are

P. Ren et al.: FDTD Analysis of Relativistic Bistatic Polarized Scattering From a High-Speed Moving Dielectric Coated Target

IEEE *Access*

plotted in Fig. 5(a)-(c), respectively. The results of the static coated cylinder are compared with the analytical solution in Fig. 5(a)-(b). It is noted that a great agreement is occured between the simulation results and the exact solution results, which demonstrated the accuracy and the efficiency of the proposed scheme for the 3D dielectric coated object. For VH-polarized scatterings, it can be observed that a significant increase and a slight increase occurred in the vicinity of the scattering angle ($\theta_s = 90°$, $\varphi_s = 0°$) and the scattering angle ($\theta_s = 270°$, $\varphi_s = 0°$), respectively. It can also be seen that the lobe width of VH-polarized RCS pattern is apparently narrowed with the increase of the velocity in the vicinity of the scattering angle ($\theta_s = 90°$, $\varphi_s = 0°$) and is also slightly narrowed as the increase of the velocity in the vicinity of the scattering angle ($\theta_s = 270°$, $\varphi_s = 0°$). In the Fig. 5(b), it can be observed that a significant right shift of the peak of the co-polarized (HH) bistatic RCS component occurred in the vicinity of the scattering angle ($\theta_s = 180°$, $\varphi_s = 0°$) and a significant left shift of the peak of the co-polarized bistatic RCS component in the vicinity of the scattering angle ($\theta_s = 360°$, $\varphi_s = 0°$). Fig. 5(c) shows the curves of RH-polarized bistatic RCS, which results from the motion of the sphere. It can be seen that RH-polarized bistatic scatterings of the cylinder increase as velocity increases. It is clear that the bistatic scatterings of the cylinder coated with the isotropic dielectric is reduced for all polarization.

C. RCS OF THE MOVING ANISOTROPIC MATERIAL COATED TARGET

For the third and fourth cases, the bistatic RCS of a moving anisotropic material coated cylinder and a moving anisotropic coated complex target are simulated, respectively.

For the case of cylinder coated with anisotropic material, the height and the radius of the cylinder are 0.608 m and 0.0748 m, respectively. The thickness of the coating material is 0.015 m. The constitutive parameters of the anisotropic material are shown as

$$\boldsymbol{\varepsilon}_r = \begin{pmatrix} 25.59 - j3.89 & 0 & 0 \\ 0 & 25.59 - j3.89 & 0 \\ 0 & 0 & 8.19 - j1.30 \end{pmatrix}$$

The incident plane wave is a plane propagating along the $y-$ axis, which is perpendicular to the motion direction of the target. The frequency of the incident plane wave is 1 GHz. Bistatic RCS versus θ_s for the target with velocities of $v = 0, 0.00001c$ (about Mach 8.82), $0.01c$, and $0.1c$ m/s are plotted in Fig. 6(a)-(f), respectively. For the VH-polarized scatterings from the coated cylinder, in the vicinity of the scattering angle ($\theta_s = 90°$, $\varphi_s = 0°$) and ($\theta_s = 270°$, $\varphi_s = 0°$), the bistatic RCS patterns almost remain the same for different velocities, even for the static PEC (Perfectly Electric Conductor) cylinder. As shown in the Fig. 6(a), as the velocity increases, the lobe width of VH-polarized RCS pattern is apparently widened and slightly narrowed in the range from ($\theta_s = 0°$, $\varphi_s = 0°$) to ($\theta_s = 180°$, $\varphi_s = 0°$) and in the range from ($\theta_s = 180°$, $\varphi_s = 0°$) to ($\theta_s = 360°$, $\varphi_s = 0°$),

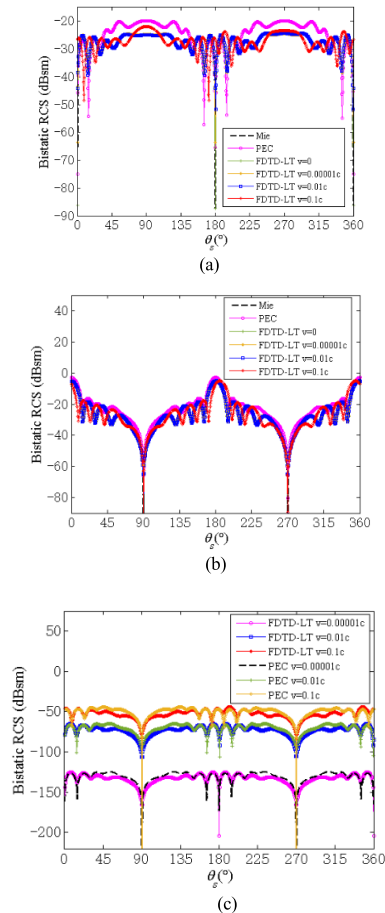**FIGURE 5.** Bistatic RCS versus scattering angle ($\theta_i = 90°$, $\varphi_i = 90°$, $\varphi_s = 0°$), (a) VH-Polarization; (b) HH-Polarization; (c) RH-Polarization.

respectively. For the HV-polarized RCS, compared to the VH-polarized RCS pattern, the characteristics of the lobe width of the bistatic RCS is more significant. Meanwhile for the crossing-polarized (HV-/VH-) scatterings, the scatterings from the coated cylinder is lower than that from PEC cylinder at most scattering angles. For the HH-polarization scattering, it can be observed that a significant right shift of the peak of the co-polarized (HH) bistatic RCS component occurred in the vicinity of the scattering angle ($\theta_s = 180°$, $\varphi_s = 0°$) and a significant left shift of the peak of the co-polarized bistatic RCS component in the vicinity of the scattering angle ($\theta_s = 360°$, $\varphi_s = 0°$). For the VV-polarized scattering, as the velocity increases, the lobe of the RCS is widened in the vicinity of scattering angles ($\theta_s = 90°$, $\varphi_s = 0°$), which is also the direction of the motion of the target. At the same time, with the increase of the velocity, the lobe of the RCS is narrowed in the vicinity of scattering angles ($\theta_s = 270°$, $\varphi_s = 0°$), which is the opposite direction of the motion of the target. For the co-polarized (VV-/HH-) scattering, compared to the HH-polarized scattering, the difference between the VV-polarized RCS results of the moving coated cylinder and that of the pec cylinder is significant.
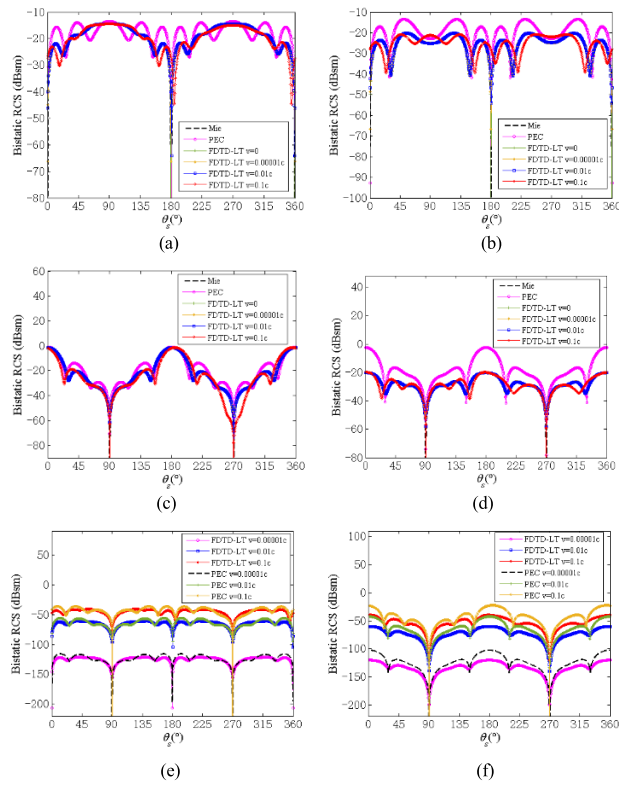
IEEE *Access*

P. Ren et al.: FDTD Analysis of Relativistic Bistatic Polarized Scattering From a High-Speed Moving Dielectric Coated Target

FIGURE 6. Bistatic RCS versus scattering angle
$(\theta_i = 90°, \varphi_i = 90°, \varphi_s = 0°)$, (a) VH-Polarization; (b) HV-Polarization;
(c) HH-Polarization; (d) VV-Polarization; (e) RH-Polarization;
(f) RV-Polarization.

Fig. 6(e)-(f) show the curves of RH-/RV-polarized bistatic RCS, which result from the motion of the sphere. It can be seen that RH-/RV-polarized bistatic scatterings of the cylinder increase as velocity increases.

Furthermore, to discuss the scattering characteristics of the moving anisotropic dielectric coated target, a moving anisotropic dielectric coated complex target is considered. The moving complex target consists of a spherical cap and a cone. As shown in Fig. 7, the axis of the cone is in the $x-$ direction. The surface of the target is slotted around the $x-$ direction at where the cone is connected to the spherical cap. The dimensions of the cone are $h = 0.608$ m and $r = 0.0748$ m. The radius of the spherical cap is $r = 0.0748$ m. The thickness of the coating material is 0.015 m. The anisotropic dielectric filled in the coating layer is the same as the above case. The incident wave is a plane wave whose propagation direction is the positive $y-$direction, which is perpendicular to the motion direction of the target. The frequency of the incident wave is 1 GHz.

The comparison of the polarized bistatic RCS of the moving anisotropic dielectric coated complex target with the velocity $v = 0, 0.00001c$ (about Mach 8.82), $0.01c$, and $0.1c$ m/s are shown in Fig. 8(a)-(f), respectively. For the HV-polarized scatterings from the anisotropic dielectric coated target, in the vicinity of the scattering angle $(\theta_s = 90°, \varphi_s = 0°)$ and $(\theta_s = 270°, \varphi_s = 0°)$, the
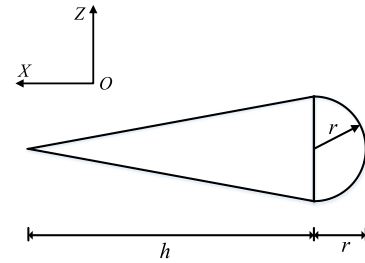

FIGURE 7. Geometry of the complex target.

bistatic RCS almost remain the same for different velocities, but is significantly higher than the RCS of the static pec target. As the target moves with the velocity of $0.1c$, a significant discrepancy occurs in the area of scattering angle $(\theta_s = 45°, \varphi_s = 0°)$, $(\theta_s = 135°, \varphi_s = 0°)$, $(\theta_s = 225°, \varphi_s = 0°)$ and $(\theta_s = 315°, \varphi_s = 0°)$. For the VH-polarized bistatic RCS, in the range from $(\theta_s = 45°, \varphi_s = 0°)$ to $(\theta_s = 135°, \varphi_s = 0°)$, bistatic RCS patterns remain almost the same for all moving speeds. In the vicinity of the scattering angle $(\theta_s = 270°, \varphi_s = 0°)$, the lobe width of VH-polarized RCS pattern is narrowed with the increase of the velocity. For the cases of co-polarized (VV, HH) scatterings, in the vicinity of the scattering angle $(\theta_s = 270°, \varphi_s = 0°)$, bistatic RCS curves remain almost the same for all moving speeds. Meanwhile, as the velocity increases, the HH-polarized RCS curves remain the same and the VV-polarized RCS curves are significantly decreasing in the vicinity of the scattering angle $(\theta_s = 90°, \varphi_s = 0°)$. As the velocity is less than $0.1c$, the co-polarized (VV, HH) and the cross-polarized (VH, HV) bistatic RCS curves are almost the same as that of the static case. It can be seen that both RV- and RH-polarized bistatic scatterings of the target increase as the velocity increases. Even if the velocity is less than $0.01c$, the curves of RV- and RH-polarized RCS corresponding to different velocities are obviously different. Meanwhile, it can be obviously seen that the co-polarized and cross-polarized bistatic RCS curves are only smaller than the RCS of the static pec target at certain angles. However, it is clear that the bistatic RCS curves of the moving complex target coated with anisotropic dielectric layer are obviously reduced for both the RV- and RH-polarization.

D. DISCUSSION OF RADIAL RADAR CROSS SECTION
In this subsection, the scattering characteristics of the radial radar cross section are discussed. From the above cases, it can be observed that both RV- and RH-polarized scatterings of any moving object are zero in the scattering direction along the moving direction or opposite direction of the target. Since the target moving along with the $+x$ axis, the scattering angles $(\theta_s = 90°, \varphi_s = 0°)$ and $(\theta_s = 270°, \varphi_s = 0°)$ denote the moving direction and opposite direction of the target, respectively. According to (24a)-(24d), when the scattering angle is $(\theta_s = 90°, \varphi_s = 0°)$, the corresponding scattering angle in the rest frame is $(\theta'_s = 90°, \varphi'_s = 0°)$.

P. Ren et al.: FDTD Analysis of Relativistic Bistatic Polarized Scattering From a High-Speed Moving Dielectric Coated Target
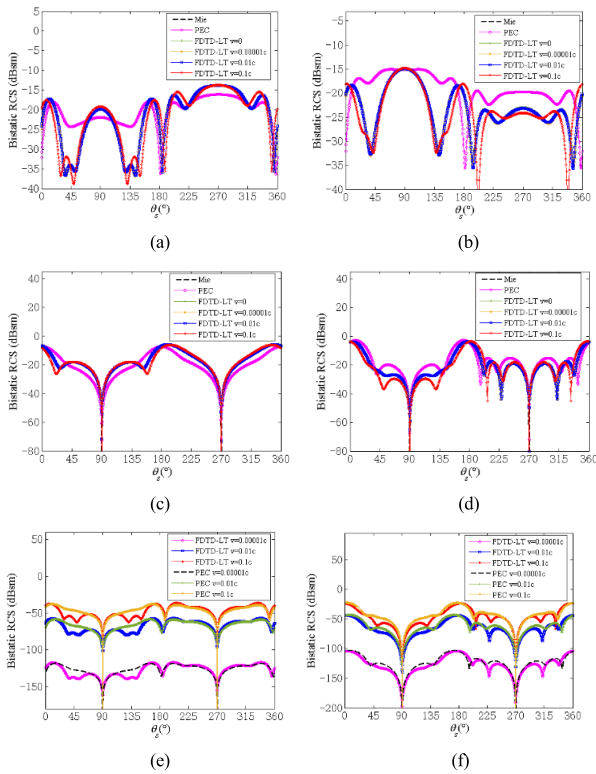
IEEE Access

FIGURE 8. Bistatic RCS versus scattering angle ($\theta_i = 90°$, $\varphi_i = 90°$, $\varphi_s = 0°$), (a) VH-Polarization; (b) HV-Polarization; (c) HH-Polarization; (d) VV-Polarization; (e) RH-Polarization; (f) RV-Polarization.

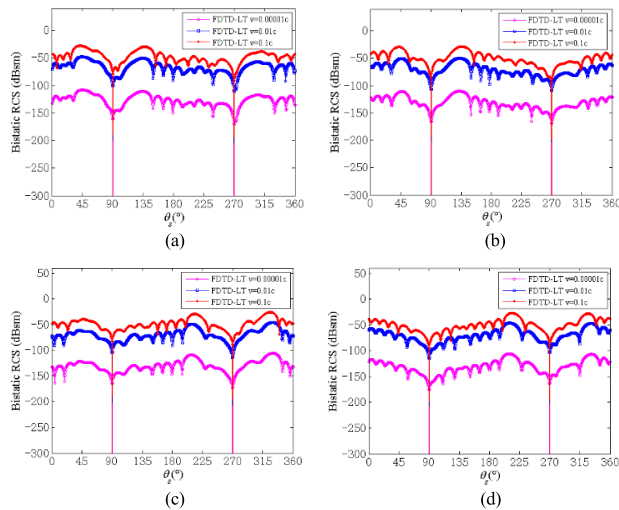**FIGURE 9.** Bistatic radial RCS versus scattering angle ($\varphi_s = 0°$), (a) RH-Polarization ($\theta_i = 60°$, $\varphi_i = 30°$); (b) RV-Polarization ($\theta_i = 60°$, $\varphi_i = 30°$); (c) RH-Polarization ($\theta_i = 45°$, $\varphi_i = 135°$); (d) RV-Polarization ($\theta_i = 45°$, $\varphi_i = 135°$).

Substituting $\left(\theta_s' = 90°, \varphi_s' = 0°\right)$ and $(\theta_s = 90°, \varphi_s = 0°)$ into (18a)-(18f), (20a)-(20c), and (21), the corresponding E_r component is equal to zero. For the case of scattering angle $(\theta_s = 270°, \varphi_s = 0°)$, the derivation of the corresponding E_r component remains the same as the scattering angle
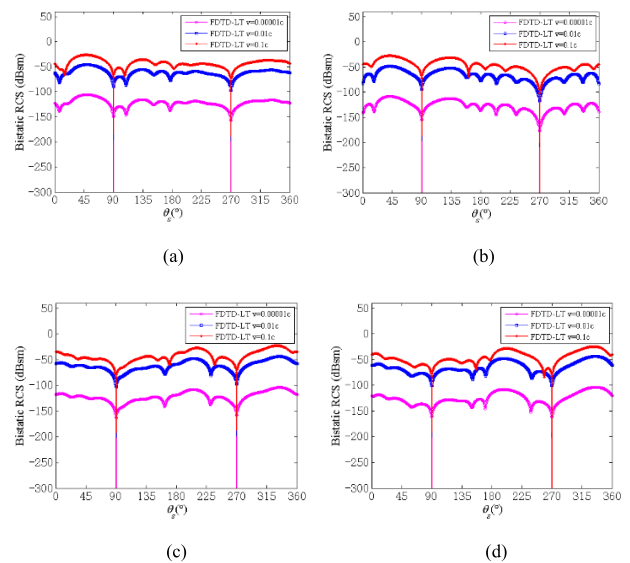

FIGURE 10. Bistatic radial RCS versus scattering angle ($\varphi_s = 0°$), (a) RH-Polarization ($\theta_i = 60°$, $\varphi_i = 30°$); (b) RV-Polarization ($\theta_i = 60°$, $\varphi_i = 30°$); (c) RH-Polarization ($\theta_i = 45°$, $\varphi_i = 135°$); (d) RV-Polarization ($\theta_i = 45°$, $\varphi_i = 135°$).

$(\theta_s = 90°, \varphi_s = 0°)$, which yields that the E_r component is still equal to zero. Thus, we can draw the conclusion that both RV- and RH-polarized scatterings of any moving object are zero in the scattering direction along the moving direction or opposite direction of the target, regardless of the incident wave propagation direction and the target itself.

Bistatic RV-/RH-polarized RCS for arbitrary incident angle of velocity $v = 0$, $0.00001c$ (about Mach 8.82), $0.01c$, and $0.1c$ m/s are shown in Figs. 9(a-d). The model used in this case is the same as the model used in Fig. 5. For the Fig. 9(a-b) and Fig. 9(c-d), the corresponding incident angles are ($\theta_i = 60°$, $\varphi_i = 30°$) and ($\theta_i = 45°$, $\varphi_i = 135°$), respectively. For the case of moving isotropic dielectric coated target, it can be seen that both RV- and RH-polarized RCS are zero in the scattering directions of ($\theta_s = 90°$, $\varphi_s = 0°$) and ($\theta_s = 270°$, $\varphi_s = 0°$) for arbitrary incident wave.

Bistatic RV-/RH-polarized RCS for the moving anisotropic dielectric coated complex target with the velocities of $v = 0$, $0.00001c$(about Mach 8.82), $0.01c$ and $0.1c$ m/s are plotted in Figs. 10(a-d). The model applied in Fig. 10 remain the same as the model used in Fig. 8. The incident angles are ($\theta_i = 60°$, $\varphi_i = 30°$) and ($\theta_i = 45°$, $\varphi_i = 135°$) for the Figs. 10(a-b) and Figs. 10(c-d), respectively. For the scattering angles ($\theta_s = 90°$, $\varphi_s = 0°$) and ($\theta_s = 270°$, $\varphi_s = 0°$), it can be observed that the radial radar cross sections of the moving anisotropic dielectric coated complex target are equal to zero for both the RV and RH polarization. Meanwhile, the conclusion that both RV- and RH-polarized scatterings of any moving object are zero in the scattering direction along the moving direction or opposite direction of the target, regardless of the incident wave propagation direction and the target itself are demonstrated through the cases of Figs. 9 and Figs. 10.

IEEE *Access*

P. Ren et al.: FDTD Analysis of Relativistic Bistatic Polarized Scattering From a High-Speed Moving Dielectric Coated Target

IV. CONCLUSION

In this paper, far-zone bistatic polarized scatterings from a moving 3D dielectric coated object have been obtained for the first time by using the combination of the extended FDTD method with the Lorentz transformation. Electromagnetic scattering of the moving dielectric coated object is almost the same as that of the static one, when the velocity is less than $0.01c$. However, as the velocity goes to $0.1c$, electromagnetic scattering pattern is distinctly different from that in the static case. It should be noted that the motion of the object leads to the radial component of scattered field in spherical coordinates system, which cannot be found for the static object. The results show that the bistatic RH-polarized RCS of object coated with dielectric is significantly reduced for different velocities, which means that the dielectric coating is still effective in reducing the radial radar cross sections. Meanwhile, it is clear that both RV- and RH-polarized scatterings of any moving object are zero in the scattering direction along the moving direction or opposite direction of the target, regardless of the incident wave propagation direction and the target itself. Radial radar cross section may be applied to recognition of moving object. In our future research, polarized scatterings from hypersonic dielectric coated stealth object will be investigated with the use of the proposed method.

REFERENCES

[1] A. Taflove, *Computational Electrodynamics: The Finite-Difference Time-Domain Method*. Norwood, MA, USA: Artech House, 1995.

[2] K. S. Yee, "Numerical solution of initial boundary value problems involving Maxwell's equations in isotropic media," *IEEE Trans. Antennas Propag.*, vol. AP-14, no. 3, pp. 302–307, May 1966.

[3] C. D. Moss, F. L. Teixeira, and J. A. Kong, "Analysis and compensation of numerical dispersion in the FDTD method for layered, anisotropic media," *IEEE Trans. Antennas Propag.*, vol. 50, no. 9, pp. 1174–1184, Sep. 2002.

[4] J. Schneider and S. Hudson, "A finite-difference time-domain method applied to anisotropic material," *IEEE Trans. Antennas Propag.*, vol. 41, no. 7, pp. 994–999, Jul. 1993.

[5] S. G. Garcia, T. M. Hung-Bao, R. G. Martin, and B. G. Olmedo, "On the application of finite methods in time domain to anisotropic dielectric waveguides," *IEEE Trans. Microw. Theory Techn.*, vol. 44, no. 12, pp. 2195–2206, Dec. 1996.

[6] A. P. Zhao, J. Juntune, and A. V. Raisanen, "An efficient FDTD algorithm for the analysis of microstrip patch antennas printed on a general anisotropic dielectric substrate," *IEEE Trans. Microw. Theory Tech.*, vol. 47, no. 7, pp. 1142–1146, 1999.

[7] H. Mosallaei and K. Sarabandi, "Magneto-dielectrics in electromagnetics: Concept and applications," *IEEE Trans Antennas Propag.*, vol. 52, pp. 1558–1567, 2004.

[8] L. Dou and A. R. Sebak, "3D FDTD method for arbitrary anisotropic materials," *Microw. Opt. Technol. Lett.*, vol. 48, no. 10, pp. 2083–2090, 2006.

[9] H. O. Lee and F. L. Teixeira, "Cylindrical FDTD analysis of LWD tools through anisotropic dipping-layered earth media," *IEEE Trans. Geosci. Remote Sens.*, vol. 45, no. 2, pp. 383–388, Feb. 2007.

[10] F. Hunsberger, R. Luebbers, and K. Kunz, "Finite-difference time-domain analysis of gyrotropic media-I: Magnetic plasma," *IEEE Trans. Antennas Propag.*, vol. 40, no. 12, pp. 1489–1495, Dec. 1992.

[11] J. A. Pereda, L. A. Vielva, A. Vegas, and A. Prieto, "A treatment of magnetized ferrites using the FDTD method," *IEEE Microw. Guided Wave Lett.*, vol. 3, no. 5, pp. 136–138, May 1993.

[12] M. Celuch, A. Moryc, and W. K. Gwarek, "Numerical stability of FDTD algorithms in gyrotropic media analysed through their dispersion relations," in *IEEE MTT-S Int. Microw. Symp. Dig.*, Jun. 2007, pp. 725–728.

[13] H. Mosallaei, "FDTD-PLRC technique for modeling of anisotropic-dispersive media and metamaterial devices," *IEEE Trans. Electromagn. Compat.*, vol. 49, no. 3, pp. 649–660, Aug. 2007.

[14] F. L. Teixeira, "Time-domain finite-difference and finite-element methods for Maxwell equations in complex media," *IEEE Trans. Antennas Propag.*, vol. 56, no. 8, pp. 2150–2166, Aug. 2008.

[15] F. Harfoush, A. Taflove, and G. A. Kriegsmann, "A numerical technique for analyzing electromagnetic wave scattering from moving surfaces in one and two dimensions," *IEEE Trans. Antennas Propag.*, vol. 37, no. 1, pp. 55–63, Jan. 1989.

[16] F. Harfoush, A. Taflove, and G. A. Kriegsmann, "Numerical implementation of relativistic electromagnetic boundary conditions in a laboratory-frame grid," *J. Comput. Phys.*, vol. 89, no. 1, pp. 80–94, Jul. 1990.

[17] L. Kuang, S. Zhu, J. Gao, Z. Zheng, and D. Dong, "A numerical method for analyzing electromagnetic scattering properties of a moving conducting object," *Int. J. Antennas Propag.*, vol. 2014, pp. 1–9, Jan. 2014.

[18] K.-S. Zheng, J.-Z. Li, G. Wei, and J.-D. Xu, "Analysis of Doppler effect of moving conducting surfaces with Lorentz-FDTD method," *J. Electromagn. Waves Appl.*, vol. 27, no. 2, pp. 149–159, Nov. 2013.

[19] K. Zheng, Z. Mu, H. Mu, and G. Wei, "Electromagnetic properties from moving dielectric in high speed with Lorentz-FDTD," *IEEE Antennas Wireless Propag. Lett.*, vol. 15, pp. 934–937, 2016.

[20] K. Zheng, X. Liu, Z. Mu, and G. Wei, "Analysis of scattering fields from moving multilayered dielectric slab illuminated by an impulse source," *IEEE Antennas Wireless Propag. Lett.*, vol. 16, pp. 2130–2133, 2017.

[21] L. Kuang, F. Xu, S. Zhu, J. Gao, and Z. Zheng, "Relativistic FDTD analysis of far-field scattering of a high-speed moving object," *IEEE Antennas Wireless Propag. Lett.*, vol. 14, pp. 879–882, 2015.

[22] K. Zheng, Y. Li, L. Xu, J. Li, and G. Wei, "Electromagnetic properties of a complex pyramid-shaped target moving at high speed," *IEEE Trans. Antennas Propag.*, vol. 66, no. 12, pp. 7472–7476, Dec. 2018.

[23] K. Zheng, Y. Li, S. Qin, K. An, and G. Wei, "Analysis of micromotion characteristics from moving conical-shaped targets using the Lorentz-FDTD method," *IEEE Trans. Antennas Propag.*, vol. 67, no. 11, pp. 7174–7179, Nov. 2019.

[24] Y. Zhao and S. Chaimool, "Relativistic finite-difference time-domain analysis of high-speed moving metamaterials," *Sci. Rep.*, vol. 8, no. 1, p. 7686, May 2018.

[25] A. Tzikas, D. Chrissoulidis, and E. Kriezis, "Relativistic bistatic scattering by a uniformly moving random rough surface," *IEEE Trans. Antennas Propag.*, vol. AP-34, no. 8, pp. 1046–1052, Aug. 1986.

[26] C. Yeh and K. F. Casey, "Reflection and transmission of electromagnetic waves by a moving dielectric slab," *Phys. Rev.*, vol. 144, no. 2, pp. 665–669, Apr. 1966.

PENGCHENG REN was born in Liaoning, China. He received the B.S. degree from East China Normal University, Shanghai, China, in 2016, where he is currently pursing the Ph.D. degree. His research interests include the numerical simulation and imaging of electromagnetic fields.

LEI KUANG (Member, IEEE) received the B.S. and M.S. degrees from Anhui University, Hefei, China, in 2001 and 2004, respectively, and the Ph.D. degree from Fudan University, Shanghai, China, in 2008. He was a Visiting Scholar with the Department of Electrical and Computer Engineering, Duke University, NC, USA, from 2016 to 2017, sponsored by China Scholarship Council. He is currently a Professor with the School of Communication and Electronic Engineering, East China Normal University, Shanghai. His current research interests include computational electromagnetics, electromagnetic scattering, and microwave imaging. He received the Excellent Instructor Award for Practical Innovation from East China Normal University in 2013.

P. Ren et al.: FDTD Analysis of Relativistic Bistatic Polarized Scattering From a High-Speed Moving Dielectric Coated Target

IEEE Access

JIANJUN GAO (Senior Member, IEEE) was born in Hebei, China, in 1968. He received the B.Eng. degree from Tsinghua University, Beijing, China, in 1991, the M.Eng. degree in microelectronics engineering from the Hebei Semiconductor Research Institute, Shijiazhuang, China, in 1994, and the Ph.D. degree in microwave engineering from Tsinghua University, in 1999. From 1999 to 2001, he was a Postdoctoral Research Fellow with the Microelectronics Research and Development Center, Chinese Academy of Sciences, Beijing, where he developed PHEMT optical modulator driver. In 2001, he joined the School of Electrical and Electronic Engineering, Nanyang Technological University, Singapore, as a Research Fellow of semiconductor device modeling and on-wafer measurement. In 2003, he joined the Institute for High Frequency and Semiconductor System Technologies, Berlin University of Technology, Berlin, Germany, as a Research Associate, where he was involved in InP HBT modeling and circuit design for high-speed optical communication. In 2004, he joined Electronics Engineering Department, Carleton University, Ottawa, ON, Canada, as a Postdoctoral Fellow of the semiconductor neural network modeling technique. From 2004 to 2007, he was a Full Professor with the Radio Engineering Department, Southeast University, Nanjing, China. Since 2007, he has been a Full Professor with the School of Information Science and Technology, East China Normal University, Shanghai, China. He has authored *RF and Microwave Modeling and Measurement Techniques for Field Effect Transistors* (SciTech, 2009), *Optoelectronic Integrated Circuit Design and Device Modeling* (Wiley, 2010), and *Heterojunction Bipolar Transistors for Circuit Design—Microwave Modeling and Parameter Extraction* (Wiley, 2015). His main research interests include characterization, modeling, and on-wafer measurement of microwave semiconductor devices, optoelectronics device, high-speed integrated circuit for radio frequency, and optical communication.

QING HUO LIU (Fellow, IEEE) received the B.S. and M.S. degrees in physics from Xiamen University, Xiamen, China, in 1983 and 1986, respectively, and the Ph.D. degree in electrical engineering from the University of Illinois at Urbana–Champaign, Champaign, IL, USA, in 1989. He was with the Electromagnetics Laboratory, University of Illinois at Urbana–Champaign, as a Research Assistant, from September 1986 to December 1988, and a Postdoctoral Research Associate, from January 1989 to February 1990. He was a Research Scientist and a Program Leader with Schlumberger-Doll Research, Ridgefield, CT, USA, from 1990 to 1995. From 1996 to May 1999, he was an Associate Professor with New Mexico State University, Las Cruces, NM, USA. Since June 1999, he has been with Duke University, Durham, NC, USA, where he is currently a Professor of electrical and computer engineering. His research interests include computational electromagnetics and acoustics, inverse problems, and their applications in nanophotonics, geophysics, biomedical imaging, and electronic packaging. He has published widely in these areas.

He is a fellow of the Acoustical Society of America, the Electromagnetics Academy, and the Optical Society of America. He received the 1996 Presidential Early Career Award for Scientists and Engineers (PECASE) from the White House, the 1996 Early Career Research Award from the Environmental Protection Agency, and the 1997 CAREER Award from the National Science Foundation. He also received the 2017 Technical Achievement Award and the 2018 Computational Electromagnetics Award from the Applied Computational Electromagnetics Society and the 2018 Harrington–Mittra Award in computational electromagnetics from the IEEE Antennas and Propagation Society. In 2018, he received the University of Illinois at Urbana–Champaign ECE Distinguished Alumni Award. He served as the Founding Editor-in-Chief for the IEEE Journal on Multiscale and Multiphysics Computational Techniques. He also served as an IEEE Antennas and Propagation Society Distinguished Lecturer.

• • •